Postselection-free controlled generation of a high-dimensional orbital-angular-momentum entangled state

Suman Karan,* Radhika Prasad, and Anand K. Jha†
Department of Physics, Indian Institute of Technology Kanpur, Kanpur, UP 208016, India

(Received 28 May 2023; revised 16 October 2023; accepted 24 October 2023; published 13 November 2023)

High-dimensional entangled states in an orbital-angular-momentum (OAM) basis offer several unique advantages for quantum information applications. However, for the optimal performance of a given application, one requires a generation technique for OAM entangled states that is completely postselection-free and fully controllable. Nonetheless, despite several efforts in the past, no such technique currently exists. In this paper, we propose just such a technique and experimentally demonstrate postselection-free generation of up to about 150-dimensional OAM entangled states. We report the generation accuracy, which is a measure of the control, to be more than 98% for states with Gaussian and triangular OAM Schmidt spectra, and up to 90% for the maximally entangled OAM states, which have rectangular spectra.

DOI: 10.1103/PhysRevApplied.20.054027

I. INTRODUCTION

A Laguerre-Gaussian (LG) mode $\mathrm{LG}_p^l(\rho,\phi)$ is characterized by indices l and p, referred to as the orbital-angular-momentum (OAM) mode index (l) and the radial mode index (p), respectively. A photon in an LG mode with index l carries OAM of $l\hbar$, where l is an integer [1]. Thus the OAM of a photon provides a discrete infinite-dimensional basis [2] as opposed to the two-dimensional polarization basis [3]. The use of high-dimensional entangled states provides higher error tolerance for quantum key distribution [4,5], higher security against eavesdropper attacks in quantum cryptographic schemes [6], increased information capacity [7,8], enhanced robustness of communication protocols in noisy environments [9,10], and stronger violations of generalized Bell's inequalities [11,12]. High-dimensional entangled states also have important implications for dense coding [13,14], quantum teleportation [15,16], entanglement swapping [17,18], and supersensitive measurements [19–21].

In the past, there have been several efforts at producing high-dimensional OAM entangled states using spontaneous parametric down-conversion (SPDC), in which a pump photon of higher frequency splits into two photons of lower frequencies, called the signal and idler. It is known that, for the optimal performance of a quantum information protocol [22,23], one needs to generate OAM entangled states in a completely postselection-free and controlled manner. However, all the past efforts have only yielded generation techniques that are either postselection-free but not fully controllable [24–27] or fully controllable but not postselection-free [11–19,28,29].

More recently, there have been experimental [30–32] and theoretical [33–35] efforts at developing generation techniques that are fully controllable but postselection-free only with respect to $p = 0$ mode detection. These techniques involve a single-mode-fiber-based OAM detection system, which mostly detects photons with radial mode index $p = 0$ [36,37]. However, it is known that the proportion of $p \neq 0$ radial modes in the OAM entangled state generated by SPDC is typically much larger than the $p = 0$ mode [38,39]. Hence, while these techniques [30–35] can have limited use in some applications, they are not postselection-free. Thus, there is no existing technique for the truly postselection-free generation of high-dimensional OAM entangled states with full control. In this paper, we experimentally demonstrate the generation of truly postselection-free OAM entangled states with control.

II. THEORY

The two-photon state generated by type-I SPDC in the transverse momentum basis can be written as [26,40,41]

$$|\psi_{\mathrm{tp}}\rangle = \iint V(\mathbf{q}_s,\mathbf{q}_i)\Phi(\mathbf{q}_s,\mathbf{q}_i)|\mathbf{q}_s\rangle_s|\mathbf{q}_i\rangle_i\, d^2\mathbf{q}_s\, d^2\mathbf{q}_i. \quad (1)$$

Here p, s, and i denote pump, signal, and idler, respectively; $V(\mathbf{q}_s,\mathbf{q}_i)$ represents the pump field amplitude; $\Phi(\mathbf{q}_s,\mathbf{q}_i)$ represents the phase-matching function; and $|\mathbf{q}_s\rangle_s$ and $|\mathbf{q}_i\rangle_i$ denote the state vectors in the transverse momentum basis of the signal and idler, respectively. In the LG

*karans@iitk.ac.in
†akjha@iitk.ac.in

basis, we can write $|\psi_{\rm tp}\rangle$ as

$$|\psi_{\rm tp}\rangle = \sum_{l_s,p_s}\sum_{l_i,p_i} C_{l_i,p_i}^{l_s,p_s}|l_s,p_s\rangle_s|l_i,p_i\rangle_i, \tag{2}$$

where l_p, l_s, and l_i are the OAM mode indices of the pump, signal, and idler, respectively [42], and $|l_s,p_s\rangle_s$ is the state of the signal photon with indices l_s and p_s, etc.

Thus, using Eqs. (1) and (2), we write $C_{l_i,p_i}^{l_s,p_s}$ as [38,43]

$$C_{l_i,p_i}^{l_s,p_s} = A\iint d^2\mathbf{q}_s\, d^2\mathbf{q}_i\, V(\mathbf{q}_s,\mathbf{q}_i)\Phi(\mathbf{q}_s,\mathbf{q}_i) \times [\mathrm{LG}_{p_s}^{l_s}(\mathbf{q}_s)]^*[\mathrm{LG}_{p_i}^{l_i}(\mathbf{q}_i)]^*, \tag{3}$$

where $\mathrm{LG}_p^l(\mathbf{q}) = \langle\mathbf{q}|l,p\rangle$ is the momentum-basis representation of the LG mode [26]. Now, using the cylindrical polar coordinates, $\mathbf{q}_s = (q_{sx},q_{sy}) = (\rho_s\cos\phi_s,\rho_s\sin\phi_s)$, $\mathbf{q}_i = (q_{ix},q_{iy}) = (\rho_i\cos\phi_i,\rho_i\sin\phi_i)$, $d^2\mathbf{q}_s = \rho_s\, d\rho_s\, d\phi_s$, and $d^2\mathbf{q}_i = \rho_i\, d\rho_i\, d\phi_i$, we write $C_{l_i,p_i}^{l_s,p_s}$ as

$$C_{l_i,p_i}^{l_s,p_s} = \int_0^\infty\int_{-\pi}^{\pi}\rho_s\rho_i\, d\rho_s\, d\rho_i\, d\phi_s\, d\phi_i\, V(\rho_s,\rho_i,\phi_s,\phi_i) \times \Phi(\rho_s,\rho_i,\phi_s,\phi_i)[\mathrm{LG}_{p_s}^{l_s}(\rho_s,\phi_s)]^*[\mathrm{LG}_{p_i}^{l_i}(\rho_i,\phi_i)]^*. \tag{4}$$

$P_{l_i}^{l_s}$ is the probability of detecting the signal and idler photons with OAM $l_s\hbar$ and $l_i\hbar$, and it is given by

$$P_{l_i}^{l_s} = \sum_{p_s=0}^{\infty}\sum_{p_i=0}^{\infty}|C_{l_i,p_i}^{l_s,p_s}|^2. \tag{5}$$

When $l_p = 0$, conservation of OAM leads to $l_s = -l_i$ [42], and, in this case, Eq. (2) takes the following Schmidt-decomposed form:

$$|\psi\rangle_{\rm tp} = \sum_l \sqrt{S_l}\,|l\rangle_s|-l\rangle_i. \tag{6}$$

Here $S_l = P_{-l}^l$ is called the OAM Schmidt spectrum. Using Eqs. (4) and (5), and employing the identity $\sum_{p=0}^{\infty}(\mathrm{LG})_p^l(\rho)(\mathrm{LG})_p^{*l}(\rho') = (1/\pi)\delta(\rho^2-\rho'^2)$ [44], we write S_l as (for a more detailed derivation, see [25]):

$$S_l = P_{-l}^l = \frac{1}{4\pi^2}\int_0^\infty\rho_s\rho_i\left|\int_{-\pi}^{\pi}V(\rho_s,\rho_i,\phi_s,\phi_i) \times \Phi(\rho_s,\rho_i,\phi_s,\phi_i)e^{-il(\phi_s-\phi_i)}\,d\phi_s\,d\phi_i\right|^2 d\rho_s\,d\rho_i. \tag{7}$$

From Eq. (7), we find that S_l is determined by the pump-field amplitude $V(\rho_s,\rho_i,\phi_s,\phi_i)$ and the phase-matching function $\Phi(\rho_s,\rho_i,\phi_s,\phi_i)$. Therefore, by selecting an appropriate $V(\rho_s,\rho_i,\phi_s,\phi_i)$ and $\Phi(\rho_s,\rho_i,\phi_s,\phi_i)$, one can generate any target OAM Schmidt spectrum. However, solving Eq. (7) to find the analytical expressions for $V(\rho_s,\rho_i,\phi_s,\phi_i)$ and $\Phi(\rho_s,\rho_i,\phi_s,\phi_i)$ for a target OAM Schmidt spectrum S_l is mathematically a very difficult problem. So, our technique for finding the required $V(\rho_s,\rho_i,\phi_s,\phi_i)$ and $\Phi(\rho_s,\rho_i,\phi_s,\phi_i)$ for a target spectrum is based on optimization and feedback.

We note that S_l expressed in Eq. (7) includes contributions from all possible radial modes since the probability $P_{l_i}^{l_s}$ in Eq. (5) has been defined as a sum over all the radial modes of the signal and idler photons. Thus S_l is the true OAM Schmidt spectrum. This is in contrast with several recent techniques [30–35], in which the spectrum is taken as the probability of only the $p = 0$ mode. We find that the spectral content observed with a $p = 0$ mode detector is only a small fraction of the true spectrum (see Appendix A for a detailed study regarding this). Thus our generation technique, which is based on measuring the S_l in Eq. (7), is truly postselection-free.

Figure 1 illustrates our technique. A Gaussian pump field with collinear phase matching provides a very limited control over generating the OAM Schmidt spectrum. However, as shown in Figure 1(b), for a controlled postselection-free generation, we use noncollinear phase matching and take the pump-field amplitude $V(\rho_s,\rho_i,\phi_s,\phi_i)$ in the form of a coherent superposition of LG modes with different p indices:

$$V(\rho_s,\rho_i,\phi_s,\phi_i) = \sum_{p=0}^{N-1}\alpha_p\,\mathrm{LG}_p^{l_p=0}(\rho_s,\rho_i,\phi_s,\phi_i), \tag{8}$$

where α_p is the complex coefficient, N is the total number of radial modes in the superposition, and

$$\mathrm{LG}_p^{l_p=0}(\rho_s,\rho_i,\phi_s,\phi_i) = \left[\frac{w_p^2}{2\pi}\right]^{1/2} L_p^0\left[\frac{w_p^2\rho_p^2}{2}\right] \times \exp\left[-\frac{w_p^2\rho_p^2}{4}\right]\exp[i\pi p]. \tag{9}$$

Here L_p^0 is the associated Laguerre polynomial, $\rho_p^2 = \rho_s^2 + \rho_i^2 + 2\rho_s\rho_i\cos(\phi_s-\phi_i)$, and w_p is the beam waist of the pump field.

The phase-matching function $\Phi(\rho_s,\rho_i,\phi_s,\phi_i)$ of Eq. (7) can be written as [25,40,41]

$$\Phi(\rho_s,\rho_i,\phi_s,\phi_i) = \mathrm{sinc}\left(\frac{\Delta k_z L}{2}\right)\exp\left[i\frac{\Delta k_z L}{2}\right], \tag{10}$$

where L is the thickness of the crystal, and Δk_z is called the phase mismatch parameter. This parameter Δk_z can be

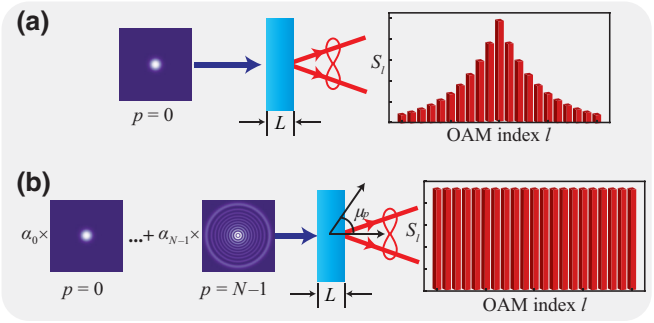

FIG. 1. (a) Generation of the OAM entangled state using a Gaussian pump-field amplitude ($\mathrm{LG}_{p=0}^{l_p=0}$) and collinear phase matching. (b) Postselection-free controlled generation of OAM entangled states with noncollinear phase matching and a pump field in the form of a superposition of modes with different radial indices.

tuned by changing the phase-matching angle θ_p, which is the angle between the propagation direction of the pump field and the optic axis of the nonlinear crystal. For the detailed expression of Δk_z, see Appendix B.

In our technique, we first numerically simulate a given OAM spectrum by optimizing the complex coefficients α_p. For a $(2D+1)$-dimensional state, we define the coefficient of determination R^2 (see Ref. [45], chapter 6) as

$$R^2 = \left[1 - \frac{\sum_{l=-D}^{+D}\left(S_l^t - S_l^o\right)^2}{\sum_{l=-D}^{+D}\left(S_l^t - \langle S_l^t\rangle\right)^2}\right] \times 100\%, \qquad (11)$$

where S_l^t and S_l^o are the target and experimentally observed OAM Schmidt spectra, and $\langle S_l^t\rangle$ is the mean of S_l^t. For a target OAM Schmidt spectrum S_l^t, we maximize R^2 by numerically optimizing α_p using a particle swarm optimization technique [46] implemented with the Python package "pyswarm." We define the maximum value of R^2,

$$\max\{R^2\} \equiv G, \qquad (12)$$

as the generation accuracy G of our technique; G quantifies the degree of control that our technique has for generating a target OAM Schmidt spectrum. Finally, we use the numerically optimized coefficients α_p as starting points for further optimizing them experimentally through a feedback mechanism.

Figure 2 presents the results of our numerical studies on how the generation accuracy G depends on the phase-matching angle θ_p, the number of radial modes N, and crystal thickness L, for three different spectra, namely, Gaussian, triangular and rectangular. The rectangular spectrum is particularly interesting in that it represents a maximally entangled state. Nonetheless, it has been shown that, for several quantum information applications, nonmaximally-entangled states are preferred over the maximally entangled states [47–49]. Therefore, we include the Gaussian and triangular spectra in our analysis.

Figure 2(a) shows the plot of G versus θ_p. For these plots, we have taken $N = 5$ and $L = 10$ mm. We find that, with the collinear phase matching condition, characterized by $\theta_p = 28.65°$, it is not possible to achieve very high values of G but, at θ_p set for sufficiently large noncollinear down-conversion, G can get close to 100% for the Gaussian and triangular spectra. However, for the rectangular spectrum, G stays much lower. The main reason for this is that one requires a larger number of radial modes N in the superposition in Eq. (8) for producing a spectrum such as rectangular which has sharp edges.

Figure 2(b) shows the numerically simulated plot of G as a function of N for $L = 10$ mm and $\theta_p = 28.71°$. We find that, as N increases, G increases. Furthermore, for Gaussian and triangular spectra, $N = 5$ is enough to get G close to 100%, whereas for the rectangular spectrum one requires at least $N = 10$ to reach $G > 95\%$. Finally, Fig. 2(c) shows the plot of G as a function of L for $N = 5$ and $\theta_p = 28.71°$. We find that, for a target spectrum, once θ_p and N have been optimized, G is not much affected by L.

III. EXPERIMENTS

The experimental setup is depicted in Fig. 3. We use a 100-mW Toptica TopMode ultraviolet (UV) continuous-wave (CW) laser of wavelength $\lambda_p = 405$ nm that is spatially filtered and incident on a Holoeye Pluto-2-UV-099 spatial light modulator (SLM). The SLM is used for generating the pump field $V(\rho_s, \rho_i, \phi_s, \phi_i)$ of Eq. (8) in the form of a superposition of N radial modes using the method described by Arrizon *et al.* [50]. For $N = 5$, we use modes from $p = 0$ to $p = 4$ with pump-beam waist $w_p = 320$ μm. The pump field is made incident on a β-barium borate (BBO) crystal of transverse dimensions 10×10 mm^2 and thickness $L = 10$ mm. The crystal is kept on a goniometer to change the phase-matching angle θ_p.

A dichroic mirror (DM) is positioned just after the crystal to block UV while allowing the down-converted photon pairs to pass through. These photon pairs are incident on a Mach-Zehnder-type interferometer [27], and the interferogram output is captured using an Andor iXon Ultra-897 electron-multiplied charged-coupled device (EMCCD) camera with 512×512 pixel grids having pixel pitch of 16×16 μm^2. Lenses with focal lengths $f_1 = 50$ mm and $f_2 = 200$ mm are placed in a $4f$ configuration to image the crystal plane with a magnification of 4. The Fourier transform of this image plane is obtained at the camera plane using another lens of focal length $f_3 = 300$ mm. For capturing the interferograms, the camera acquisition time is

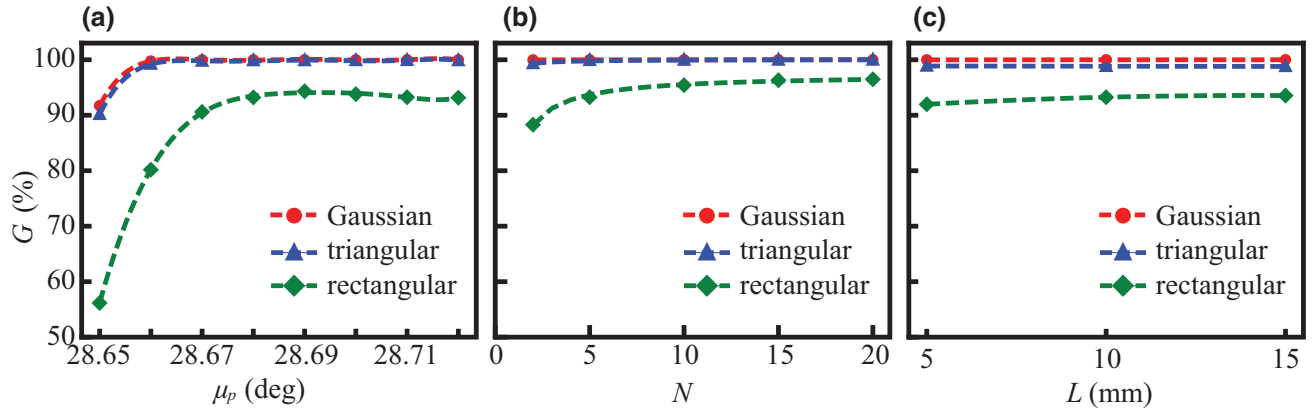

FIG. 2. Numerical plots of the dependence of generation accuracy G for three different OAM Schmidt spectra: Gaussian, triangular, and rectangular. (a) Plot of G as a function of the phase-matching angle θ_p for $N = 5$ and $L = 10$ mm. (b) Plot of G as a function of the maximum number of radial modes N for $L = 10$ and $\theta_p = 28.71°$. (c) Plot of G as a function of the crystal thickness L for $N = 5$ and $\theta_p = 28.71°$. Dashed lines denote the best fit.

kept at 20 s. An interference filter (IF) of central wavelength 810 nm and bandwidth 10 nm is placed in front of the camera.

For a target spectrum S_I^t, we use the optimized complex coefficients α_p from our numerical simulations as the starting point and produce the pump field $V(\rho_s, \rho_i, \phi_s, \phi_i)$ using the SLM. We then experimentally observe the generated spectrum S_I^o with the EMCCD using the two-shot technique described in Ref. [27] and calculate R^2 using Eq. (11). We then employ manual feedback in order to obtain an optimized set of α_p that maximizes R^2. For the optimization, we take α_p one-by-one, optimize its real and imaginary parts first in steps of ± 0.1, and then in smaller steps. The experimentally observed value of R^2 after optimization is then taken as the generation accuracy G.

We note that the strength of the pump field hitting the BBO crystal is only about 5 mW. We find that, at this field strength, the relative probability of generating a four-photon state versus a two-photon state is less than 10^{-7} [51]. Therefore, the contribution due to four-photon effects in our experiment is negligible. We further note that, although our technique is postselection-free in the OAM basis, the two-photon generation in time is only probabilistic due to the pump field being CW.

Figure 4 presents our experimental results. Figures 4(a), 4(b), and 4(c) show the experimentally generated Gaussian, triangular and rectangular OAM Schmidt spectra with

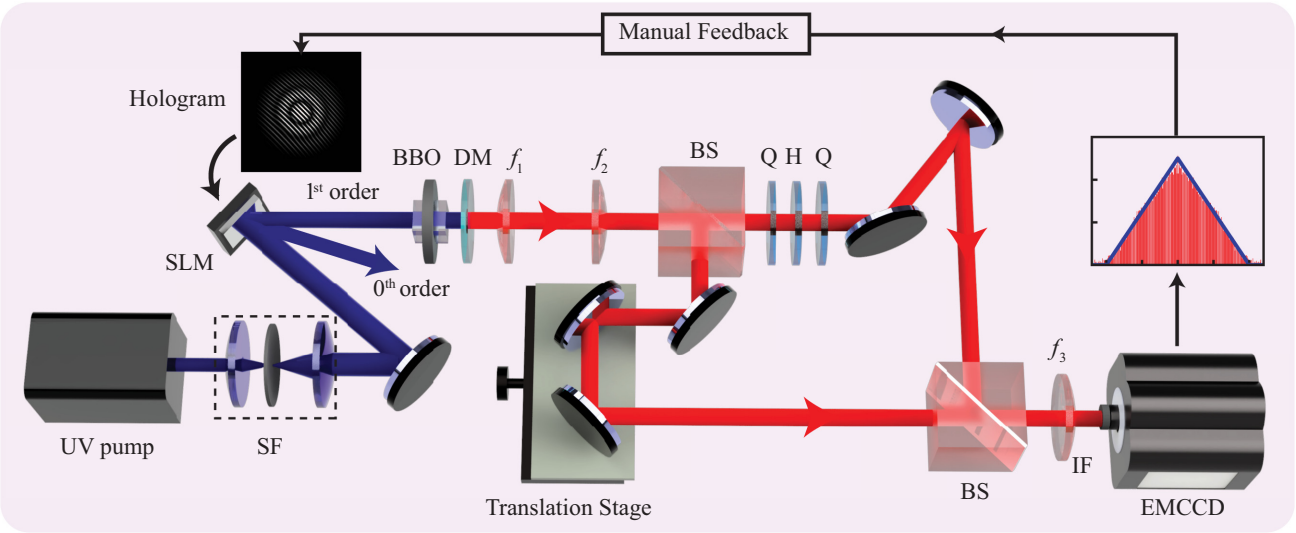

FIG. 3. Schematic of the experimental setup: SF, spatial filter; SLM, spatial light modulator; BBO, β-barium borate crystal; DM, dichroic mirror; BS, 50:50 nonpolarization beam splitter; Q, quarter-wave plate; H, half-wave plate; and IF, interference filter of central wavelength 810 nm and 10 nm frequency bandwidth.

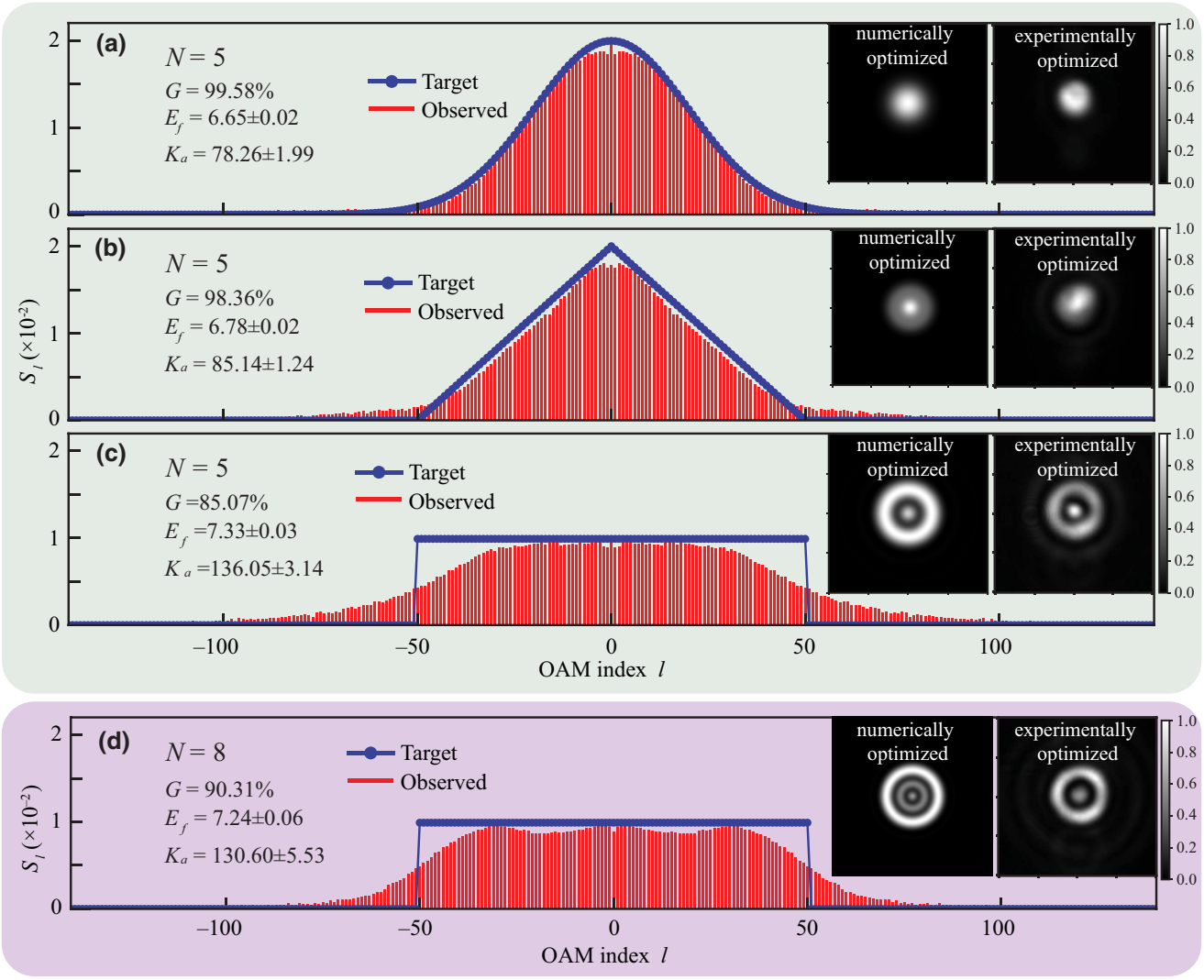

FIG. 4. Experimentally generated OAM Schmidt spectra. (a)–(c) Plots of target and experimentally observed OAM Schmidt spectra having (a) Gaussian, (b) triangular and (c) rectangular shapes with $L = 10$ mm, $\theta_p = 28.71°$, and $N = 5$. (d) Plot of target and experimentally observed rectangular OAM Schmidt spectrum with $L = 10$ mm, $\theta_p = 28.71°$, and $N = 8$. In all panels, the insets show the pump-field intensities after the initial numerical and then the final experimental optimizations.

$N = 5$. The pump-field intensities for the three spectra after numerical optimization and then final experimental optimization are shown as insets and the superposition coefficients α_p after the final experimental optimization are reported in Appendix D. The target standard deviation of the Gaussian spectrum is 20, while the target full width of the triangular and rectangular spectra is 100.

In order to verify that the states produced above are entangled, we use entanglement of formation E_f as a certifier [52]. An $E_f > 0$ confirms that the state is entangled. We note that when the two-photon state is mixed, certifying entanglement through E_f requires measuring correlations in at least two conjugate bases [53,54]. More recently, it has been shown that even the quantification of entanglement of high-dimensional mixed states can be done through only two measurements [55]. However, for the case of pure two-photon states, entanglement can be verified by measuring correlation in only one basis [52,56] or of only one of the photons [57,58]. In our technique, we use a spatially completely coherent pump field, which ensures that the generated two-photon state is pure [59–61]. Therefore, we calculate E_f using the formula $E_f = -\sum_l S_l \log_2 S_l$ for the three spectra and find it to be 6.65 ± 0.02, 6.78 ± 0.02, and 7.33 ± 0.03.

The Schmidt number K_a quantifies the dimensionality of generated sates and is calculated using the formula $K_a = 1/\sum_l S_l^2$ [44]. For the three different target spectra reported in Figs. 4(a), 4(b), and 4(c), the corresponding Schmidt numbers are 78.26 ± 1.99, 85.14 ± 1.24, and 136.05 ± 3.14, respectively. The generation accuracy G for the

three spectra is 99.58%, 98.36%, and 85.07%, respectively. From the results presented in Figs. 4(a)–(c), we find that there is always a difference between the numerically and experimentally optimized coefficients. This is because the numerically optimized results are for the ideal conditions, but, in a real experiment, the conditions are usually quite different from being ideal. We also note that for the Gaussian and triangular spectra, G is more than 98%, while for the rectangular spectrum, G is only about 85%. As shown in Fig. 2, and also pointed out in Sec. II on theory, the main reason for the lower G value for the rectangular spectrum is that a much larger N is required for producing a spectrum such as rectangular that has sharp edges. Although $N = 5$ is sufficient for producing Gaussian and triangular spectra with almost perfect accuracy, one needs larger N for producing a rectangular spectrum.

Therefore, for the rectangular spectrum, we next perform experiments with $N = 8$ radial modes, ranging from $p = 0$ to $p = 7$. The other experimental details remain the same as mentioned above. Figure 4(d) shows the experimentally generated spectrum. The optimized coefficients are reported in Appendix D. The experimentally measured values of G, E_f, and K_a are 90.31%, 7.24 ± 0.06, and 130.60 ± 5.53, respectively. We note that, with $N = 8$ modes, G for the rectangular spectrum becomes more than 90%. A further increase in N can increase G even further.

However, the maximum N that can be implemented is limited by two main factors. One is that, as we increase the radial mode index p, the transverse size of the pump beam increases. As a result, for a given transverse size of the nonlinear crystal, we can only use a finite number of radial modes, and this puts an upper limit on N. Although one can increase N by reducing the beam waist and thereby fitting more radial modes, a reduced pump-beam waist results in a larger spread of the pump beam [59], making it difficult to capture the entire down-converted field by the detection system. The other factor is the algorithm for optimizing α_p. In our experiment, the optimization of α_p involves manual feedback. Therefore, increasing N implies increasing the number of iterations in the feedback process and thereby increasing the experimental complexity and overall noise. Nevertheless, a feedback mechanism with automated controls can make the optimization much more efficient. Therefore, with a nonlinear crystal with larger transverse size and an automated feedback mechanism, a much higher generation accuracy, even for a sharp-edged spectrum, should be easily achievable with our technique.

Finally, in order to highlight the control provided by our technique, we perform experiments with three different L, namely $L = 5$ mm, $L = 10$ mm, and $L = 15$ mm, for producing Gaussian, triangular, and rectangular spectra with two different spectral widths (see Appendixes C, D, and E for details). We find that different crystal thickness requires different phase-matching conditions. Therefore, by optimizing θ_p and α_p, one can generate a given target OAM

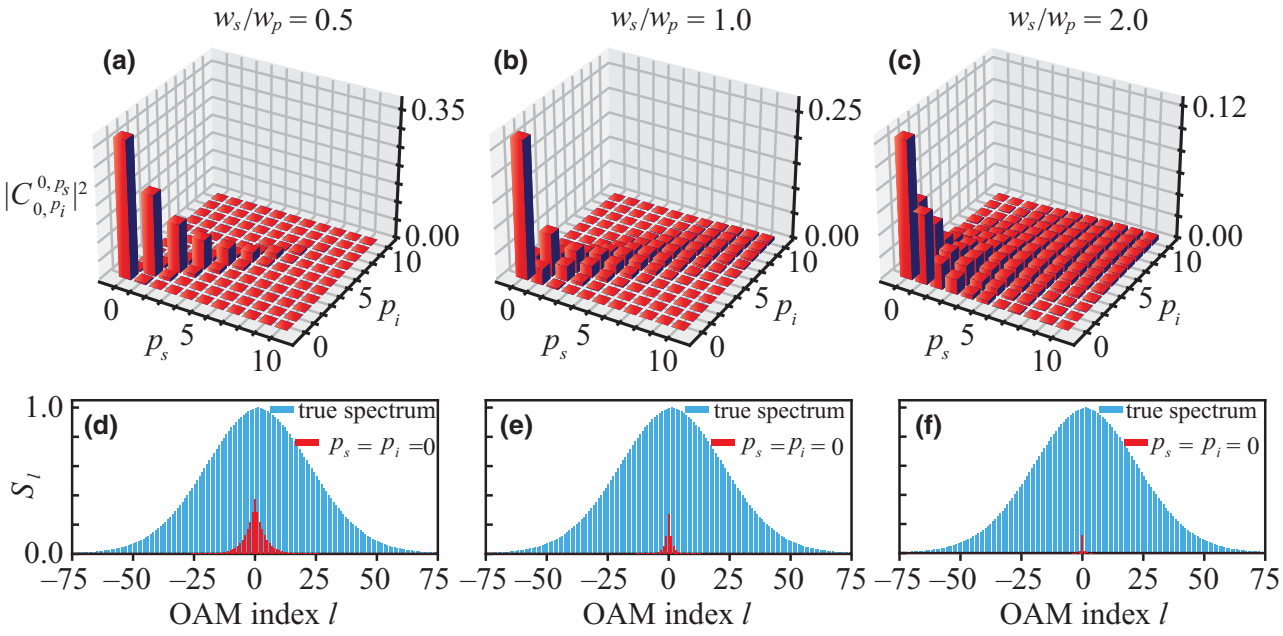

FIG. 5. The extent of postselection in detection techniques based on selecting only the $p = 0$ mode. (a)–(c) Plots of C^{0,p_s}_{0,p_i} for $w_s/w_p = 0.5$, 1, and 2, respectively. (d)–(f) Plots of the true Schmidt spectrum for $w_s/w_p = 0.5$, 1, and 2, respectively. For the above plots, we have taken $L = 10$ mm, $\theta_p = 28.71°$, and $w_p = 320$ μm.

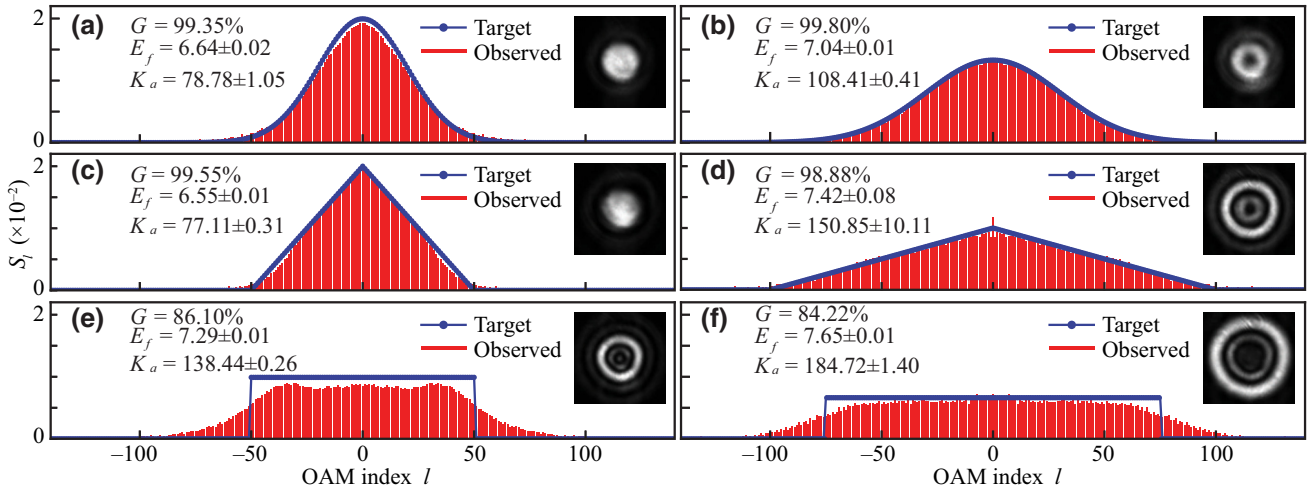

FIG. 6. Target and experimentally observed OAM Schmidt spectra with $L = 5$ mm and $\theta_p = 28.69°$ with two separate widths for the target: (a),(b) Gaussian spectra, (c),(d) triangular spectra, and (e),(f) rectangular spectra. The pump-field intensities after the final experimental optimization are shown in the insets.

spectrum for a wide range of crystal thickness. The only implication is that the optimization complexity becomes different at different crystal thickness. In Appendixes C, D, and E, we report the generation of states with target dimensionality up to 200. By increasing θ_p, the dimensionality of the generated state can be further increased, which ultimately becomes limited by the collection aperture of the detection system.

IV. CONCLUSION

In conclusion, we have proposed and demonstrated an experimental technique based on SPDC for postselection-free controlled generation of up to about 150-dimensional OAM entangled states. Ours is the first truly postselection-free technique for generating OAM entangled states with full control. We note that the main limitation of our technique is that it works only for the OAM entangled states in the Schmidt-decomposed form. This is due to the fact that currently there is no efficient detector for measuring a general OAM entangled state. With the advent of such a detector, our technique could in principle be extended to general OAM entangled states. Furthermore, it has been shown that for several quantum information applications non-maximally-entangled states are preferred over the maximally entangled states [47–49]. Thus, our work can have important implications for high-dimensional quantum information.

ACKNOWLEDGMENTS

We thank Girish Kulkarni and Manik Banik for helpful discussions. We acknowledge financial support from the Science and Engineering Research Board through grants STR/2021/000035 and CRG/2022/003070 and from the Department of Science & Technology, Government of India, through Grant DST/ICPS/QuST/Theme-1/2019). S.K. thanks the University Grant Commission (UGC), Government of India, for financial support.

APPENDIX A: EXTENT OF POSTSELECTION IN TECHNIQUES BASED ON DETECTING $p = 0$ RADIAL MODE

We have seen that $|C^{l_s,p_s}_{l_i,p_i}|^2$ is the probability of detecting the signal and idler photons in LG modes with indices (l_s, p_s) and (l_i, p_i), respectively. The expression for $C^{l_s,p_s}_{l_i,p_i}$ is

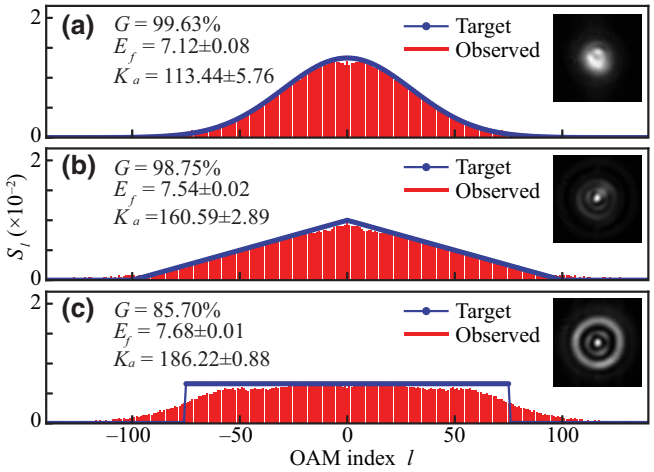

FIG. 7. Target and experimentally observed OAM Schmidt spectra with $L = 10$ mm and $\theta_p = 28.71°$ for the target: (a) Gaussian spectrum, (b) triangular spectrum, and (c) rectangular spectrum. The pump-field intensities after the final experimental optimization are shown in the insets.

TABLE I. Optimized superposition coefficients (α_p) for $L = 5$ mm.

Spectrum	Width	Complex coefficients				
		α_0	α_1	α_2	α_3	α_4
Gaussian	20	$-0.68 - 0.68i$	$0.14 + 0.01i$	$0.00 + 0.00i$	$0.24 + 0.00i$	$0.00 + 0.00i$
	30	$-0.56 - 0.56i$	$0.31 - 0.31i$	$0.00 + 0.00i$	$0.44 + 0.00i$	$0.01 + 0.00i$
triangular	100	$-0.93 - 0.09i$	$-0.13 + 0.00i$	$0.22 - 0.13i$	$-0.20 + 0.01i$	$0.00 + 0.00i$
	200	$0.04 + 0.34i$	$-0.55 - 0.04i$	$0.42 - 0.13i$	$-0.04 - 0.46i$	$0.00 + 0.42i$
rectangular	100	$0.23 + 0.11i$	$-0.56 - 0.09i$	$-0.23 - 0.05i$	$0.18 - 0.07i$	$0.25 - 0.68i$
	150	$0.14 + 0.00i$	$-0.39 + 0.04i$	$0.71 - 0.32i$	$-0.28 + 0.21i$	$0.14 + 0.28i$

given in Eq. (4), where $\mathrm{LG}_{p_s}^{l_s}(\rho_s, \phi_s)$ is the projection mode for the signal photon. We write $\mathrm{LG}_{p_s}^{l_s}(\rho_s, \phi_s)$ as

$$\mathrm{LG}_{p_s}^{l_s}(\rho_s, \phi_s) = \left[\frac{w_s^2 p_s!}{2\pi\,(|l_s| + p_s)!}\right]^{1/2} \left[\frac{w_s \rho_s}{\sqrt{2}}\right]^{|l_s|} L_{p_s}^{|l_s|} \times \left[\frac{w_s^2 \rho_s^2}{2}\right] \exp\left[-\frac{w_s^2 \rho_s^2}{4}\right] \times \exp\left[i l_s \phi_s + i\pi\left(p_s - \frac{|l_s|}{2}\right)\right], \quad \text{(A1)}$$

where $L_{p_s}^{|l_s|}[\cdots]$ is called the associated Laguerre polynomial, and w_s is the beam waist of the projected mode basis in which the signal photon is being detected. The $\mathrm{LG}_{p_i}^{l_i}(\rho_i, \phi_i)$ in Eq. (4) has a similar expression. We take $w_i = w_s$ and calculate $|C_{-l,p_i}^{l,p_s}|^2$ using Eq. (4).

Figures 5(a), 5(b), and 5(c) show the numerically calculated plots of $|C_{0,p_i}^{0,p_s}|^2$ as functions of p_s and p_i for $w_s/w_p = 0.5$, 1, and 2, respectively. We take $L = 10$ mm, $\theta_p = 28.71^\circ$, and $w_p = 320$ μm. We normalize $|C_{0,p_i}^{0,p_s}|^2$ within the space $p_s = 0$ to $p_s = 10$, and $p_i = 0$ to $p_i = 10$, such that the total probability is equal to one. Next, Figs. 5(d), 5(e), and 5(f) show the plots of OAM Schmidt spectra S_l as functions of l calculated using two different methods. One is the true Schmidt spectrum S_l, which contains contributions due to all the radial modes. It is derived in Eq. (7) and is given by

$$S_l = P_{-l}^{l} = \sum_{p_s=0}^{\infty} \sum_{p_i=0}^{\infty} |C_{-l,p_i}^{l,p_s}|^2.$$

The other one is the probability $|C_{-l,p_i=0}^{l,p_s=0}|^2$, which contains contributions only due to the $p_s = 0$ and $p_i = 0$ modes. We find that the OAM Schmidt spectrum observed with a detection scheme that is sensitive only to $p = 0$ modes [30–35] entails strong postselection, and that the extent of this postselection increases with increasing w_s/w_p.

APPENDIX B: CALCULATION OF THE PHASE MISMATCH PARAMETER

The phase-matching function in Eq. (10) is defined as $\Phi(\rho_s, \rho_i, \phi_s, \phi_i) = \mathrm{sinc}(\Delta k_z L/2) \exp[i(\Delta k_z L)/2]$. Here Δk_z is called the phase mismatch parameter and is given by [40]

$$\Delta k_z = k_{sz} + k_{iz} - k_{pz}, \quad \text{(B1)}$$

where

$$k_{pz} = -\alpha_p q_{px} + \eta_p K_{p0} - \frac{[\beta_p^2 q_{px}^2 + \gamma_p^2 q_{py}^2]}{2\eta_p K_{p0}},$$

$$k_{sz} = n_{so} K_{s0} - \frac{1}{2n_{so}K_{s0}}(q_{sx}^2 + q_{sy}^2),$$

$$k_{iz} = n_{io} K_{i0} - \frac{1}{2n_{io}K_{i0}}(q_{ix}^2 + q_{iy}^2).$$

Here k_{sz} represents the z component of the wave vector for the signal field, etc.; $K_{j0} = 2\pi/\lambda_j$ with $j = s, i, p$; and n_{jo} and n_{je} are the refractive indices for the ordinary and extraordinary polarizations. For type-I SPDC, the polarization of the pump photon is extraordinary while those of the

TABLE II. Optimized superposition coefficients (α_p) for $L = 10$ mm.

Spectrum	Width	Complex coefficients				
		α_0	α_1	α_2	α_3	α_4
Gaussian	20	$0.21 + 0.94i$	$-0.13 + 0.19i$	$-0.09 - 0.01i$	$-0.01 - 0.03i$	$0.03 - 0.02i$
	30	$-0.46 - 0.71i$	$0.43 - 0.22i$	$0.06 + 0.20i$	$-0.04 + 0.06i$	$-0.05 - 0.03i$
triangular	100	$0.55 - 0.57i$	$0.47 - 0.31i$	$-0.12 - 0.12i$	$-0.14 - 0.05i$	$-0.07 - 0.02i$
	200	$0.32 + 0.36i$	$-0.10 - 0.68i$	$-0.10 + 0.04i$	$-0.04 - 0.01i$	$-0.51 - 0.15i$
rectangular	100	$-0.69 + 0.15i$	$0.39 - 0.10i$	$0.39 - 0.34i$	$0.22 - 0.09i$	$-0.01 + 0.11i$
	150	$0.11 + 0.18i$	$-0.44 - 0.59i$	$0.04 + 0.26i$	$0.48 + 0.34i$	$-0.02 - 0.02i$

TABLE III. Optimized superposition coefficients (α_p) with $L = 10$ mm and $N = 8$ reported in Fig. 4(d).

Complex coefficients	
α_0	$-0.08 + 0.68i$
α_1	$-0.01 - 0.37i$
α_2	$0.33 - 0.36i$
α_3	$-0.01 - 0.20i$
α_4	$-0.08 - 0.09i$
α_5	$0.18 + 0.00i$
α_6	$-0.19 + 0.12i$
α_7	$-0.10 + 0.09i$

signal and idler photons are ordinary. The quantities α_p, β_p, γ_p, and η_p are given by

$$\alpha_p = \frac{(n_{po}^2 - n_{pe}^2)\sin\theta_p\cos\theta_p}{n_{po}^2\sin^2\theta_p + n_{pe}^2\cos^2\theta_p},$$

$$\beta_p = \frac{n_{po}n_{pe}}{n_{po}^2\sin^2\theta_p + n_{pe}^2\cos^2\theta_p},$$

$$\gamma_p = \frac{n_{po}}{\sqrt{n_{po}^2\sin^2\theta_p + n_{pe}^2\cos^2\theta_p}},$$

$$\eta_p = \frac{n_{po}n_{pe}}{\sqrt{n_{po}^2\sin^2\theta_p + n_{pe}^2\cos^2\theta_p}}.$$

In our experiment, we use a BBO crystal for down-conversion, and the values of n_{po} and n_{pe} for BBO can be obtained from the dispersion relation reported in Ref. [62]. For degenerate SPDC, we can write $K_{s0} \approx K_{i0} \approx K_{p0}/2$ and $n_{so} = n_{io}$. Numerically, we find that for our experimental parameters, $\alpha_p \approx 0$ and $\beta_p \approx \gamma_p \approx 1$. Thus, Δk_z can be written in the transverse momentum basis as

$$\Delta k_z = K_{p0}[n_{so} - \eta_p] - \frac{1}{2\eta_p K_{p0}}[\rho_s^2 + \rho_i^2 - 2\rho_s\rho_i\cos(\phi_s - \phi_i)]. \quad \text{(B2)}$$

APPENDIX C: EXPERIMENTAL RESULTS WITH $L = 5$ mm

In this section, we report our experimental results with $L = 5$ mm, $\theta_p = 28.69°$, and $N = 5$. Figures 6(a) and 6(b) show the target and experimentally observed Gaussian OAM Schmidt spectra with standard deviations 20 and 30. Figures 6(c) and 6(d) are the OAM Schmidt spectra of triangular shapes with base widths 100 and 200. The rectangular spectrum of widths 100 and 150 are reported in Figs. 6(e) and 6(f), respectively. The intensity profiles of the pump field for each spectrum are shown as insets, and the corresponding α_p values are presented in Table I. Experimentally obtained K_a, E_f, and G for each generated OAM Schmidt spectrum are reported in the respective figures.

APPENDIX D: EXPERIMENTAL RESULTS WITH $L = 10$ mm

In this section, we report our experimental results with $L = 10$ mm, $\theta_p = 28.71°$, and $N = 5$. Figures 7(a), 7(b), and 7(c) show the plots of target and experimentally observed S_l for a Gaussian spectrum with standard deviation 30, a triangular spectrum with base width 200, and a rectangular spectrum of width 150. The spatial intensity profiles of the pump field for each spectrum are shown as insets, and the corresponding α_p values are presented

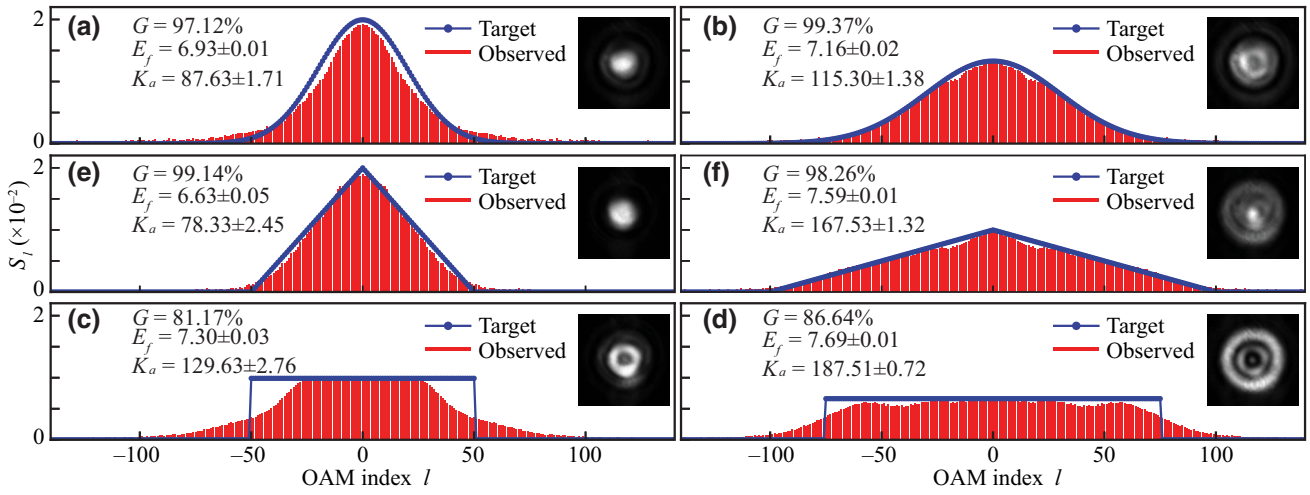

FIG. 8. Target and experimentally observed OAM Schmidt spectra with $L = 15$ mm and $\theta_p = 28.71°$ with two separate widths for the target: (a),(b) Gaussian spectra, (c),(d) triangular spectra, and (e),(f) rectangular spectra. The pump-field intensities after the final experimental optimization are shown in the insets.

TABLE IV. Optimized superposition coefficients (α_p) for $L = 15$ mm.

Spectrum	Width	Complex coefficients				
		α_0	α_1	α_2	α_3	α_4
Gaussian	20	$-0.17 + 0.82i$	$0.34 - 0.03i$	$0.34 - 0.03i$	$-0.17 + 0.00i$	$-0.20 + 0.03i$
	30	$-0.78 + 0.43i$	$0.31 - 0.03i$	$0.25 - 0.03i$	$-0.17 + 0.00i$	$-0.14 + 0.03i$
triangular	100	$0.19 + 0.97i$	$0.02 + 0.01i$	$-0.09 - 0.09i$	$0.06 + 0.06i$	$-0.01 + 0.02i$
	200	$0.03 + 0.32i$	$-0.87 - 0.03i$	$0.03 - 0.15i$	$-0.15 - 0.26i$	$0.00 + 0.15i$
rectangular	100	$0.83 + 0.00i$	$0.31 + 0.18i$	$-0.14 + 0.13i$	$0.00 + 0.35i$	$0.00 + 0.18i$
	150	$0.20 + 0.20i$	$-0.83 + 0.00i$	$0.22 - 0.23i$	$0.10 - 0.33i$	$-0.10 - 0.02i$

in Table II, which also provides the optimized α_p values for a Gaussian spectrum of standard deviation 20, a triangular spectrum of base width 100, and a rectangular spectrum with width 100. In Fig. 4(d), we reported our observations with $L = 10$ mm and $N = 8$. The corresponding superposition coefficients α_p are reported in Table III.

APPENDIX E: EXPERIMENTAL RESULTS WITH $L = 15$ mm

In this section, we report our experimental results with $L = 15$, $\theta_p = 28.71^\circ$, and $N = 5$. Figures 8(a) and 8(b) show the target and experimentally observed Gaussian OAM Schmidt spectra with standard deviations 20 and 30. Figures 8(c) and 8(d) are the OAM Schmidt spectra of triangular shapes with base widths 100 and 200. The rectangular spectrum of widths 100 and 150 are reported in Figs. 8(e) and 8(f), respectively. The spatial intensity profiles of the pump field are shown as insets, and the corresponding α_p values are presented in Table IV.

[1] L. Allen, M. W. Beijersbergen, R. J. C. Spreeuw, and J. P. Woerdman, Orbital angular momentum of light and the transformation of Laguerre-Gaussian laser modes, Phys. Rev. A **45**, 8185 (1992).

[2] A. M. Yao and M. J. Padgett, Orbital angular momentum: Origins, behavior and applications, Adv. Opt. Photonics **3**, 161 (2011).

[3] A. Forbes and I. Nape, Quantum mechanics with patterns of light: Progress in high dimensional and multidimensional entanglement with structured light, AVS Quantum Sci. **1**, 011701 (2019).

[4] H. Bechmann-Pasquinucci and A. Peres, Quantum Cryptography with 3-State Systems, Phys. Rev. Lett. **85**, 3313 (2000).

[5] G. M. Nikolopoulos, K. S. Ranade, and G. Alber, Error tolerance of two-basis quantum-key-distribution protocols using qudits and two-way classical communication, Phys. Rev. A **73**, 032325 (2006).

[6] N. J. Cerf, M. Bourennane, A. Karlsson, and N. Gisin, Security of Quantum Key Distribution using d-Level Systems, Phys. Rev. Lett. **88**, 127902 (2002).

[7] J. Wang, J.-Y. Yang, I. M. Fazal, N. Ahmed, Y. Yan, H. Huang, Y. Ren, Y. Yue, S. Dolinar, M. Tur, and A. E. Willner, Terabit free-space data transmission employing orbital angular momentum multiplexing, Nat. Photonics **6**, 488 (2012).

[8] N. Bozinovic, Y. Yue, Y. Ren, M. Tur, P. Kristensen, H. Huang, A. E. Willner, and S. Ramachandran, Terabit-scale orbital angular momentum mode division multiplexing in fibers, Science **340**, 1545 (2013).

[9] S. Ecker, F. Bouchard, L. Bulla, F. Brandt, O. Kohout, F. Steinlechner, R. Fickler, M. Malik, Y. Guryanova, R. Ursin, and M. Huber, Overcoming Noise in Entanglement Distribution, Phys. Rev. X **9**, 041042 (2019).

[10] F. Zhu, M. Tyler, N. H. Valencia, M. Malik, and J. Leach, Is high-dimensional photonic entanglement robust to noise?, AVS Quantum Sci. **3**, 011401 (2021).

[11] J. Leach, B. Jack, J. Romero, M. Ritsch-Marte, R. W. Boyd, A. K. Jha, S. M. Barnett, S. Franke-Arnold, and M. J. Padgett, Violation of a Bell inequality in two-dimensional orbital angular momentum state-spaces, Opt. Express **17**, 8287 (2009).

[12] A. C. Dada, J. Leach, G. S. Buller, M. J. Padgett, and E. Andersson, Experimental high-dimensional two-photon entanglement and violations of generalized Bell inequalities, Nat. Phys. **7**, 677 (2011).

[13] F. Wang, M. Erhard, A. Babazadeh, M. Malik, M. Krenn, and A. Zeilinger, Generation of the complete four-dimensional Bell basis, Optica **4**, 1462 (2017).

[14] X.-M. Hu, Y. Guo, B.-H. Liu, Y.-F. Huang, C.-F. Li, and G.-C. Guo, Beating the channel capacity limit for superdense coding with entangled ququarts, Sci. Adv. **4**, eaat9304 (2018).

[15] Y.-H. Luo, H.-S. Zhong, M. Erhard, X.-L. Wang, L.-C. Peng, M. Krenn, X. Jiang, L. Li, N.-L. Liu, C.-Y. Lu, A. Zeilinger, and J.-W. Pan, Quantum Teleportation in High Dimensions, Phys. Rev. Lett. **123**, 070505 (2019).

[16] X.-M. Hu, C. Zhang, B.-H. Liu, Y. Cai, X.-J. Ye, Y. Guo, W.-B. Xing, C.-X. Huang, Y.-F. Huang, C.-F. Li, and G.-C. Guo, Experimental High-Dimensional Quantum Teleportation, Phys. Rev. Lett. **125**, 230501 (2020).

[17] Y. Zhang, M. Agnew, T. Roger, F. S. Roux, T. Konrad, D. Faccio, J. Leach, and A. Forbes, Simultaneous entanglement swapping of multiple orbital angular momentum states of light, Nat. Commun. **8**, 632 (2017).

[18] S. Takeda, M. Fuwa, P. van Loock, and A. Furusawa, Entanglement Swapping Between Discrete and Continuous Variables, Phys. Rev. Lett. **114**, 100501 (2015).

[19] A. K. Jha, G. S. Agarwal, and R. W. Boyd, Supersensitive measurement of angular displacements using entangled photons, Phys. Rev. A **83**, 053829 (2011).

[20] L. Chen, J. Lei, and J. Romero, Quantum digital spiral imaging, Light: Sci. Appl. **3**, e153 (2014).

[21] S. Asban, K. E. Dorfman, and S. Mukamel, Quantum phase-sensitive diffraction and imaging using entangled photons, Proc. Natl. Acad. Sci. **116**, 201904839 (2019).

[22] F. Bouchard, K. Heshami, D. England, R. Fickler, R. W. Boyd, B.-G. Englert, L. L. Sánchez-Soto, and E. Karimi, Experimental investigation of high-dimensional quantum key distribution protocols with twisted photons, Quantum **2**, 111 (2018).

[23] Y. Ding, D. Bacco, K. Dalgaard, X. Cai, X. Zhou, K. Rottwitt, and L. K. Oxenløwe, High-dimensional quantum key distribution based on multicore fiber using silicon photonic integrated circuits, Npj Quantum Inf. **3**, 25 (2017).

[24] H. D. L. Pires, H. C. B. Florijn, and M. P. van Exter, Measurement of the Spiral Spectrum of Entangled Two-Photon States, Phys. Rev. Lett. **104**, 020505 (2010).

[25] G. Kulkarni, L. Taneja, S. Aarav, and A. K. Jha, Angular Schmidt spectrum of entangled photons: Derivation of an exact formula and experimental characterization for noncollinear phase matching, Phys. Rev. A **97**, 063846 (2018).

[26] J. P. Torres, A. Alexandrescu, and L. Torner, Quantum spiral bandwidth of entangled two-photon states, Phys. Rev. A **68**, 050301 (2003).

[27] G. Kulkarni, R. Sahu, O. S. Magaña-Loaiza, R. W. Boyd, and A. K. Jha, Single-shot measurement of the orbital-angular-momentum spectrum of light, Nat. Commun. **8**, 1054 (2017).

[28] X.-L. Wang, X.-D. Cai, Z.-E. Su, M.-C. Chen, D. Wu, L. Li, N.-L. Liu, C.-Y. Lu, and J.-W. Pan, Quantum teleportation of multiple degrees of freedom of a single photon, Nature **518**, 516 (2015).

[29] A. Vaziri, J.-W. Pan, T. Jennewein, G. Weihs, and A. Zeilinger, Concentration of Higher Dimensional Entanglement: Qutrits of Photon Orbital Angular Momentum, Phys. Rev. Lett. **91**, 227902 (2003).

[30] S. Liu, Z. Zhou, S. Liu, Y. Li, Y. Li, C. Yang, Z. Xu, Z. Liu, G. Guo, and B. Shi, Coherent manipulation of a three-dimensional maximally entangled state, Phys. Rev. A **98**, 062316 (2018).

[31] S. Liu, Y. Zhang, C. Yang, S. Liu, Z. Ge, Y. Li, Y. Li, Z. Zhou, G. Guo, and B. Shi, Increasing two-photon entangled dimensions by shaping input-beam profiles, Phys. Rev. A **101**, 052324 (2020).

[32] E. V. Kovlakov, S. S. Straupe, and S. P. Kulik, Quantum state engineering with twisted photons via adaptive shaping of the pump beam, Phys. Rev. A **98**, 060301 (2018).

[33] N. Bornman, W. T. Buono, M. Lovemore, and A. Forbes, Optimal pump shaping for entanglement control in any countable basis, Adv. Quantum Technol. **4**, 2100066 (2021).

[34] C. Xu, L. Xiao, J. He, H. Zhang, D. Wei, X. Hu, M. Xiao, and Y. Zhang, Manipulating the radial components of LG pump beam for ultrahigh-dimensional maximally entangled orbital angular momentum states, Opt. Express **30**, 11120 (2022).

[35] F. Miatto, D. Giovannini, J. Romero, S. Franke-Arnold, S. Barnett, and M. Padgett, Bounds and optimisation of orbital angular momentum bandwidths within parametric down-conversion systems, Eur. Phys. J. D **66**, 1 (2012).

[36] H. Qassim, F. M. Miatto, J. P. Torres, M. J. Padgett, E. Karimi, and R. W. Boyd, Limitations to the determination of a Laguerre–Gauss spectrum via projective, phase-flattening measurement, J. Opt. Soc. Am. B **31**, A20 (2014).

[37] G. P. Agrawal, in *Nonlinear Science at the Dawn of the 21st Century* (Springer Berlin Heidelberg), p. 195.

[38] F. M. Miatto, A. M. Yao, and S. M. Barnett, Full characterization of the quantum spiral bandwidth of entangled biphotons, Phys. Rev. A **83**, 033816 (2011).

[39] Y. Zhang, F. S. Roux, M. McLaren, and A. Forbes, Radial modal dependence of the azimuthal spectrum after parametric down-conversion, Phys. Rev. A **89**, 043820 (2014).

[40] S. Karan, S. Aarav, H. Bharadhwaj, L. Taneja, A. De, G. Kulkarni, N. Meher, and A. K. Jha, Phase matching in β-barium borate crystals for spontaneous parametric down-conversion, J. Opt. **22**, 083501 (2020).

[41] S. Walborn, C. Monken, S. Pádua, and P. S. Ribeiro, Spatial correlations in parametric down-conversion, Phys. Rep. **495**, 87 (2010).

[42] A. Mair, A. Vaziri, G. Weihs, and A. Zeilinger, Entanglement of the orbital angular momentum states of photons, Nature **412**, 313 (2001).

[43] A. M. Yao, Angular momentum decomposition of entangled photons with an arbitrary pump, New J. Phys. **13**, 053048 (2011).

[44] A. K. Jha, G. S. Agarwal, and R. W. Boyd, Partial angular coherence and the angular Schmidt spectrum of entangled two-photon fields, Phys. Rev. A **84**, 063847 (2011).

[45] S. A. Glantz and B. K. Slinker, *Primer of Applied Regression & Analysis of Variance* (McGraw-Hill, New York, 2001), Vol. 654.

[46] M. R. Bonyadi and Z. Michalewicz, Particle swarm optimization for single objective continuous space problems: A review, Evol. Comput. **25**, 1 (2017).

[47] S. Bandyopadhyay and A. Ghosh, Optimal fidelity for a quantum channel may be attained by nonmaximally entangled states, Phys. Rev. A **86**, 020304 (2012).

[48] A. Acín, S. Massar, and S. Pironio, Randomness Versus Nonlocality and Entanglement, Phys. Rev. Lett. **108**, 100402 (2012).

[49] M. Alimuddin, A. Chakraborty, G. L. Sidhardh, R. K. Patra, S. Sen, S. R. Chowdhury, S. G. Naik, and M. Banik, Advantage of Hardy's nonlocal correlation in reverse zero-error channel coding, arXiv preprint arXiv:2303.06848 (2023).

[50] V. Arrizón, U. Ruiz, R. Carrada, and L. A. González, Pixelated phase computer holograms for the accurate encoding of scalar complex fields, J. Opt. Soc. Am. A **24**, 3500 (2007).

[51] J. Schneeloch, S. H. Knarr, D. F. Bogorin, M. L. Levangie, C. C. Tison, R. Frank, G. A. Howland, M. L. Fanto, and P. M. Alsing, Introduction to the absolute brightness and number statistics in spontaneous parametric down-conversion, J. Opt. **21**, 043501 (2019).

[52] C. H. Bennett, H. J. Bernstein, S. Popescu, and B. Schumacher, Concentrating partial entanglement by local operations, Phys. Rev. A **53**, 2046 (1996).
[53] S. Hill and W. K. Wootters, Entanglement of a Pair of Quantum Bits, Phys. Rev. Lett. **78**, 5022 (1997).
[54] W. K. Wootters, Entanglement of Formation of an Arbitrary State of Two Qubits, Phys. Rev. Lett. **80**, 2245 (1998).
[55] Y. Li, S.-Y. Huang, M. Wang, C. Tu, X.-L. Wang, Y. Li, and H.-T. Wang, Two-Measurement Tomography of High-Dimensional Orbital Angular Momentum Entanglement, Phys. Rev. Lett. **130**, 050805 (2023).
[56] W. K. Wootters, Entanglement of formation and concurrence., Quantum Inf. Comput. **1**, 27 (2001).
[57] A. Bhattacharjee, N. Meher, and A. K. Jha, Measurement of two-photon position–momentum Einstein–Podolsky–Rosen correlations through single-photon intensity measurements, New J. Phys. **24**, 053033 (2022).
[58] S. Walborn, P. Souto Ribeiro, L. Davidovich, F. Mintert, and A. Buchleitner, Experimental determination of entanglement with a single measurement, Nature **440**, 1022 (2006).
[59] A. K. Jha and R. W. Boyd, Spatial two-photon coherence of the entangled field produced by down-conversion using a partially spatially coherent pump beam, Phys. Rev. A **81**, 013828 (2010).
[60] G. Kulkarni, P. Kumar, and A. K. Jha, Transfer of temporal coherence in parametric down-conversion, J. Opt. Soc. Am. B **34**, 1637 (2017).
[61] G. Kulkarni, V. Subrahmanyam, and A. K. Jha, Intrinsic upper bound on two-qubit polarization entanglement predetermined by pump polarization correlations in parametric down-conversion, Phys. Rev. A **93**, 063842 (2016).
[62] D. Eimerl, L. Davis, S. Velsko, E. K. Graham, and A. Zalkin, Optical, mechanical, and thermal properties of barium borate, J. Appl. Phys. **62**, 1968 (1987).